First observations of SO_2 from the satellite Suomi NPP OMPS: Widespread air pollution events over China

Kai Yang,[1,2] Russell R. Dickerson,[1] Simon A. Carn,[3] Cui Ge,[4] and Jun Wang[4]

Received 17 August 2013; accepted 9 September 2013; published 19 September 2013.

[1] Severe smog episodes over China in January 2013 received worldwide attention. This air pollution was distinguished by heavy loadings of fine particulate matter and SO_2. To characterize these episodes, we employed the Ozone Mapping and Profiler Suite, Nadir Mapper (OMPS NM), an ultraviolet (UV) spectrometer flying on the Suomi National Polar-orbiting Partnership (SNPP) spacecraft since October 2011. We developed an advanced algorithm to quantify SO_2 in the lower troposphere and achieved high-quality retrievals from OMPS NM, which are characterized by high precision, ~0.2 Dobson Units (DU; 1 DU = 2.69×10^{16} molecules/cm^2) for instantaneous field of view SO_2 data and low biases (within ±0.2 DU). Here we report SO_2 retrievals and UV aerosol index data for these pollution events. The SO_2 columns and the areas covered by high pollutant concentrations are quantified; the results reveal for the first time the full extent (an area of ~10^6 km^2 containing up to 60 kt of SO_2) of these episodes. **Citation:** Yang, K., R. R. Dickerson, S. A. Carn, C. Ge, and J. Wang (2013), First observations of SO_2 from the satellite Suomi NPP OMPS: Widespread air pollution events over China, *Geophys. Res. Lett.*, *40*, 4957–4962, doi:10.1002/grl.50952.

1. Introduction

[2] The recent winter air pollution episodes over China, as publicized by news reports of sustained dense smog that engulfed Beijing in January 2013, are among the worst in history, rivaling the deadly Great Smog of London in 1952 [*Thorsheim*, 2009] and the suffocating photochemical smog of Los Angeles [*Haagen-Smit*, 1952] in the 1940s to 1970s. The largest sources of air pollutants in China are coal combustion and motor vehicle exhausts [*He et al.*, 2002], which, respectively, were also the major culprits of the historical London and LA smogs. China's fast growing economy, as evidenced by its rapid industrialization and urbanization, is predominantly powered by its abundant supplies of coal, which accounts for about 70% of China's total energy consumption [*U.S. Energy Information Administration*, 2012]. In addition to greenhouse gas (carbon dioxide, CO_2) emission, coal burning releases significant amounts of air pollutants, including sulfur dioxide (SO_2), nitrogen oxides (NOx = NO + NO_2), carbon monoxide (CO), mercury (Hg), and fine particles (i.e., smoke). The gaseous pollutants, SO_2 and NOx, are usually oxidized in the air and combine with water vapor to form sulfuric and nitric acid aerosols, which may be further mixed with the emitted smoke, ammonia, as well as dust from the deserts of Mongolia and China; this type of mixture is usually the main component of winter smog over eastern China [*Tao et al.*, 2012].

[3] Anthropogenic SO_2 is the key signature of air pollution in China, and its column density serves as a proxy for the concentration of pollutants coemitted from fossil fuel combustion. This is especially true in the winter months, when relatively low-tech heating by burning coal contributes a large proportion of air pollutants. These pollutants are usually released into the planetary boundary layer (PBL) but may be subsequently lofted into the free troposphere by the winter cold fronts from the Siberian high [*Wang et al.*, 2004; *Dickerson et al.*, 2007] and transported over long distances [*Hsu et al.*, 2012]. A synoptic perspective on the severity and extent of air pollution can be obtained using spaceborne ultraviolet (UV) instruments, capable of detecting its signature component, SO_2, in the lower atmosphere [*Eisinger and Burrows*, 1998; *Krotkov et al.*, 2006; *Carn et al.*, 2007; *Lee et al.*, 2008; *Nowlan et al.*, 2011] and providing daily global coverage to monitor its evolution and transport. In this paper we report the first SO_2 measurements using the new UV Ozone Mapping and Profiler Suite (OMPS) Nadir Mapper (NM) instrument, launched into orbit on 28 October 2011 onboard the Suomi National Polar-orbiting Partnership (SNPP) spacecraft. We describe the first observations of SO_2 from SNPP/OMPS, quantify the daily loadings, estimate the spatial extent, and characterize the evolution of the January 2013 air pollution events over China.

2. Retrievals From OMPS NM

[4] Suomi NPP/OMPS NM is a nadir-viewing hyperspectral instrument that measures backscattered ultraviolet radiance spectra in the 300–380 nm wavelength range at a resolution of 1 nm (defined as the full width at half maximum (FWHM) of the spectral response function) and a sampling rate of 2.4 pixels per FWHM. It is in a Sun-synchronous, low Earth orbit, with a local ascending (northbound) equator crossing time at 1:30 P.M. Contiguous daily global coverage is delivered using a two-dimensional charge-coupled device (CCD) detector array that covers a 2800 km cross-track swath (110° field of view, FOV) with a nadir pixel size of 50 × 50 km, attributed to the heritage of the Total Ozone Mapping Spectrometer missions

[1]Department of Atmospheric and Oceanic Science, University of Maryland College Park, College Park, Maryland, USA.
[2]Atmospheric Chemistry and Dynamics Laboratory, NASA Goddard Space Flight Center, Greenbelt, Maryland, USA.
[3]Department of Geological and Mining Engineering and Sciences, Michigan Technological University, Houghton, Michigan, USA.
[4]Department of Earth and Atmospheric Sciences, University of Nebraska Lincoln, Lincoln, Nebraska, USA.

Corresponding author: K. Yang, Atmospheric Chemistry and Dynamics Laboratory, Code 614, NASA Goddard Space Flight Center, 8800 Greenbelt Rd., Greenbelt, MD 20771, USA. (Kai.Yang-1@nasa.gov)

©2013. American Geophysical Union. All Rights Reserved.
0094-8276/13/10.1002/grl.50952

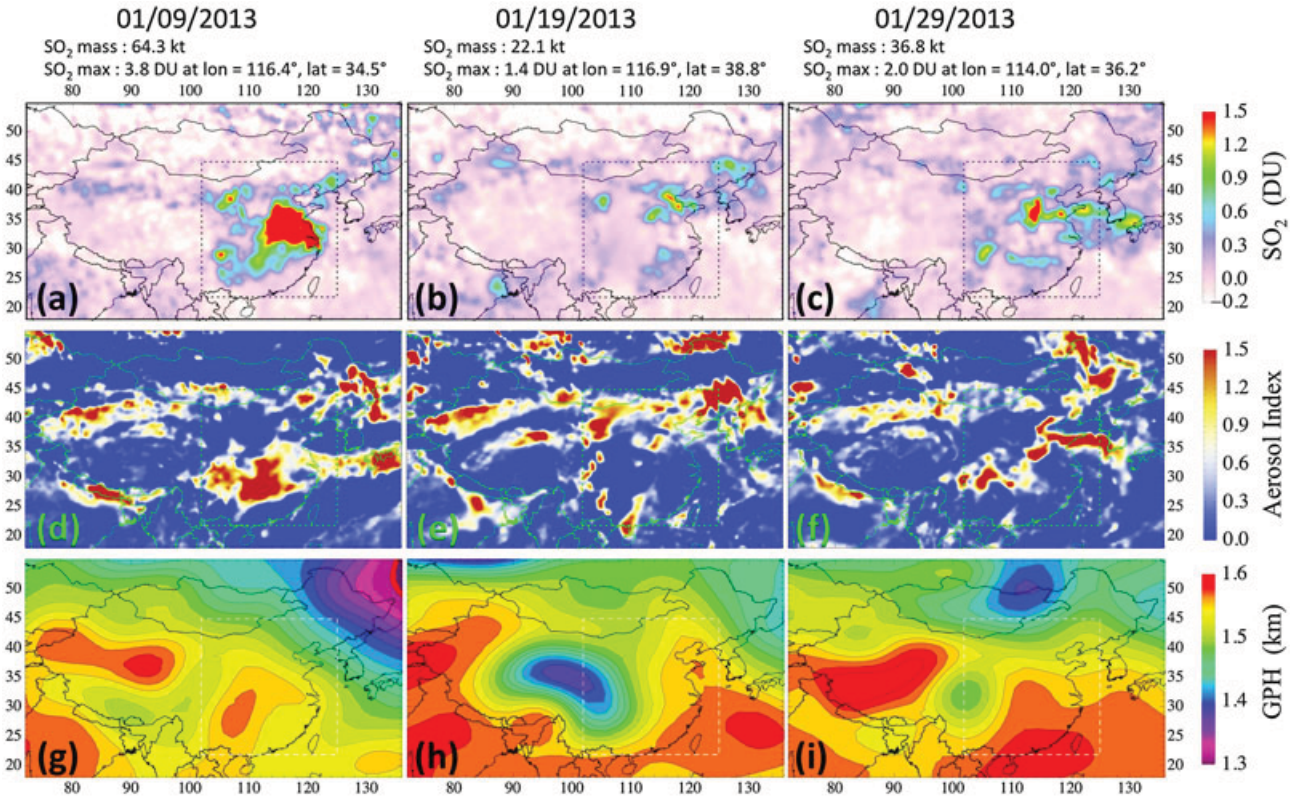

Figure 1. Maps of SO_2 vertical column (VCD) density and aerosol index (AI) from OMPS iterative spectral fitting (ISF) retrievals for 3 days in January 2013. (a–c) The SO_2 loading, maximum SO_2 VCD, and its corresponding location displayed above each SO_2 map. The loading is computed as the total SO_2 mass observed within the dashed square area on the map, with lower left corner at 101.9°E, 21.8°N and the upper right corner at 125.0°E and 44.9°N. (g–i) The NCEP reanalysis 850 hPa geopotential height (GPH in kilometers) at 06:00 UTC for these 3 days. Note that the full swaths of the OMPS observations are used in producing these daily maps, without filtering based on surface albedo, cloud fraction, or viewing angles. Only a few pixels with low retrieval quality are excluded from the maps.

[*Heath et al.*, 1975; *Fleig et al.*, 1982]. The improved performance of OMPS NM includes high signal-to-noise ratio (e.g., ∼1500 at 310 nm) radiance measurements using a single detector array to cover the entire measured spectral range; hence, it is uniquely suitable for SO_2 measurements. In contrast, the predecessors of OMPS NM, including the Global Ozone Monitoring Experiment (GOME) [*Burrows et al.*, 1999] on the European Remote Sensing Satellite-2 (ERS-2), the Scanning Imaging Absorption Spectrometer for Atmospheric Chartography (SCIAMACHY) on Environmental Satellite [*Bovensmann et al.*, 1999], the Ozone Monitoring Instrument (OMI) on Aura [*Levelt et al.*, 2006], and GOME2 [*Munro et al.*, 2006] on MetOp-A and B, measured earthshine radiance using three or more spectral channels to cover a broader wavelength range at higher sampling frequencies and narrower spectral resolutions. For SCIAMACHY, OMI, and GOME-2, there is a channel split near 310 nm. Consequently, the measured radiance spectra of these instruments in the channel-overlap region (extending a few nanometers either side of 310 nm) are degraded and are in general not used in SO_2 retrievals, even though this region is highly sensitive to SO_2 in the PBL. We also stress that OMPS NM is currently the only operational UV satellite instrument providing contiguous daily global coverage at low- to midlatitudes, due to data gaps in the OMI and GOME-2 measurements.

[5] To take advantage of the hyperspectral UV measurements and reduce the impact of measurement noise, in order to extract more reliable geophysical information, we refine and apply the iterative spectral fitting (ISF) algorithm developed by *Yang et al.* [2009, 2010] to OMPS NM radiance spectra between 308 and 345 nm. This spectral range is divided into two subwindows in the iterative fitting process, 308–333 nm and 333–345 nm. The former is used to derive the amounts of O_3 and SO_2 constrained by the respective climatological O_3 [*Bhartia and Wellemeyer*, 2002] and SO_2 [*Lee et al.*, 2009] profiles, while the latter is used for determination of spectral surface reflectivity or cloud fraction. Specifically, we use the Mixed Lambert-Equivalent Reflectivity (MLER) model [*Ahmad et al.*, 2004] to account for the effects of partial cloud and/or aerosol detected in the OMPS instantaneous FOV (IFOV), and the MLER cloud pressure is simultaneously retrieved by adjusting it until the calculated Rotational Raman Scattering filling-in factor [*Joiner et al.*, 1995] matches the corresponding measurement. This pressure is usually lower than that of the ground surface and represents the level of an opaque surface that reproduces the combined reflection of the ground surface and scattering particles (clouds and/or aerosols) in the atmosphere. The lower the MLER pressure, the higher the altitude of these scattering particles in the atmosphere. Using this simultaneously derived cloud pressure and cloud fraction

facilitates the proper treatment of the partial shielding of trace gasses located below the scattering particles, as well as the enhancement of trace gasses located at higher altitudes.

[6] The precision of the PBL SO_2 data from the OMPS ISF retrieval is about 0.2 Dobson Units (DU; 1 DU = 2.69×10^{16} molecules/cm^2), estimated from the standard deviation of background SO_2 measurements. However, it is more difficult to quantify the ISF SO_2 retrieval accuracy, which is mainly determined by two factors: the vertical distribution of SO_2 and the presence of cloud and/or aerosol. A mismatch between the climatological and the true SO_2 profiles, as well as a difference in the modeled and the actual mean paths of photons backscattered to the satellite sensor, can lead to retrieval errors, especially in the presence of cloud and/or aerosols. The ISF retrieval using OMI data has been validated against in situ aircraft measurements in China [*He et al.*, 2012]. It was found that ISF retrievals yield accurate quantification of SO_2 when the concentration is high and is more accurate than retrievals using the band residual difference method [*Krotkov et al.*, 2006]. Frequently, the mass loading of a geographic region is aggregated from many satellite IFOVs. In this case, because the errors associated from profile shape assumptions and cloud/aerosol effects may cancel out in the summation, the uncertainty in the total is usually much smaller than that of the individual measurements and is estimated to be less than 10% when the total SO_2 mass loading is greater than 10 kilotons (kt).

[7] In addition to O_3 and SO_2 columns, the ISF retrieval provides useful information on atmospheric conditions and the underlying surface at the time of observation. The UV aerosol index (AI), proportional to the slope of spectral reflectivity [*Yang et al.*, 2009 and 2010] in an IFOV, is also obtained from the retrieved MLER parameters. A positive AI value indicates the presence of UV absorbing aerosols: dust, smoke, or both. Thus, UV satellite measurements can potentially provide coincident information on O_3, SO_2, NO_2, and particulate matter, which represent four of the six criteria air pollutants identified by the US Environmental Protection Agency.

3. Results: SO_2 and Smog Episodes

[8] The wealth of information retrieved from OMPS NM measurements and its daily global coverage provide a unique synoptic perspective on episodic air pollution events. Here we demonstrate this capability of monitoring global atmospheric environments with the first quantification of air pollution over China in January 2013.

[9] The air quality related geophysical parameters are displayed in Figure 1, which show maps of SO_2 vertical column density (VCD) in DU and AI over East Asia, retrieved from OMPS observations for 3 days in January 2013. The SO_2 maps reveal the spatial distribution of this air pollutant, one of the main components of smog. Similarly, the AI maps (Figures 1d–1f) display the geographic distribution of UV-absorbing aerosols. These patterns suggest that both local aerosols (smoke and urban/industrial aerosols) and dust blown from the Taklimakan and Gobi deserts of western China contribute to the aerosol load in eastern China. The 3 days selected for Figure 1 represent dates with heavy (Figure 1a), light (Figure 1b), and moderate (Figure 1c) SO_2 loadings. For the day with a high loading, the map (Figure 1a) shows the widespread distribution of SO_2, blanketing a large portion of eastern China; a high-pressure system (Figure 1g) that suppressed atmospheric dispersion in the region likely contributed to heavy smog. In contrast, on the days with medium and low loadings, hot spots of air pollution remain, such as in the Sichuan Basin and Beijing area (surrounded by mountains to the west, north, and northeast). These hot spots occurred persistently during this month, indicating the strength of local sources and/or effects of local topography and meteorology. However, under the synoptic conditions that are dominated by the midlatitude trough (Figures 1h and 1i), large-scale high loadings of SO_2 are unlikely to occur. The maps also reveal the typical trajectories of air pollution outflow: the northeast flow path (Figure 1b) via high midlatitude large eddy systems and the east flow path (Figure 1c) via the prevalent subtropical-midlatitude westerly winds.

[10] To chart the evolution of air pollution in January 2013, we show in Figure 2 the daily SO_2 loadings (Figure 2a), the extent of heavily SO_2 polluted areas (Figure 2b, full bars), and smog-covered areas (Figure 2b, sub (red) bars). The smog-covered areas are subsets of heavily SO_2 (>0.5 DU) polluted regions, in which the UV AI is also high (>1). The time series in Figure 2 shows four distinctive, synoptic-scale air pollution episodes. The first one was the longest, lasting for 12 days from the beginning of January. During the first episode, high SO_2 loadings, often mixed with high levels of UV-absorbing aerosols, covered a large portion of eastern China. Additional large-scale episodes occurred in 14 to 16 January, 21 to 24 January, and from 28 to 30 January, respectively. There was a more localized smog episode, affecting the Beijing and Tianjin regions and their vicinity, which occurred in 18 and 19 January.

[11] Daily satellite observations provide snapshots of SO_2 spatial distributions, not only influenced by the source of emissions but also strongly affected by the local meteorological conditions and topography. The recurrent satellite overpasses allow time averaging of these instantaneous measurements, yielding a stable spatial distribution that relates more closely to the locations and fluxes of the emission sources [*Fioletov et al.*, 2011]. Figure 3a shows the average SO_2 VCD map derived from OMPS NM observations with less than 50% cloud cover (i.e., MLER cloud fraction <0.5) in the IFOVs over East Asia for January 2013. The highest average OMPS VCDs (>1 DU) are all located just south and southeast of Beijing, distributed within three provinces (Shandong, Hebei, and Henan), indicating that SO_2 emissions from these provinces are the major contributors to air pollution in January. These high concentrations of SO_2 were likely intensified by synoptic anomalies, including a weaker Siberian high and a localized high-pressure anomaly over northeast China (Figure 3c), which resulted in persistent higher relative humidity, higher temperature, and weaker winds that favor the formation of smog. Moderately elevated SO_2 concentrations are also evident in Liaoning, Jiangsu, Shanxi, and Sichuan/Chongqing provinces, signifying the locations of additional sources of air pollutants. Lastly, isolated and low-level enhancements of SO_2 above the background are detected in Hubei province, Ningxia Region, and Urumqi in Xinjiang Region, representing weaker emissions sources that contributed to the widespread distribution of these air pollution episodes.

[12] To evaluate the OMPS SO_2 retrievals, we show in Figure 3b the corresponding average OMI SO_2 map,

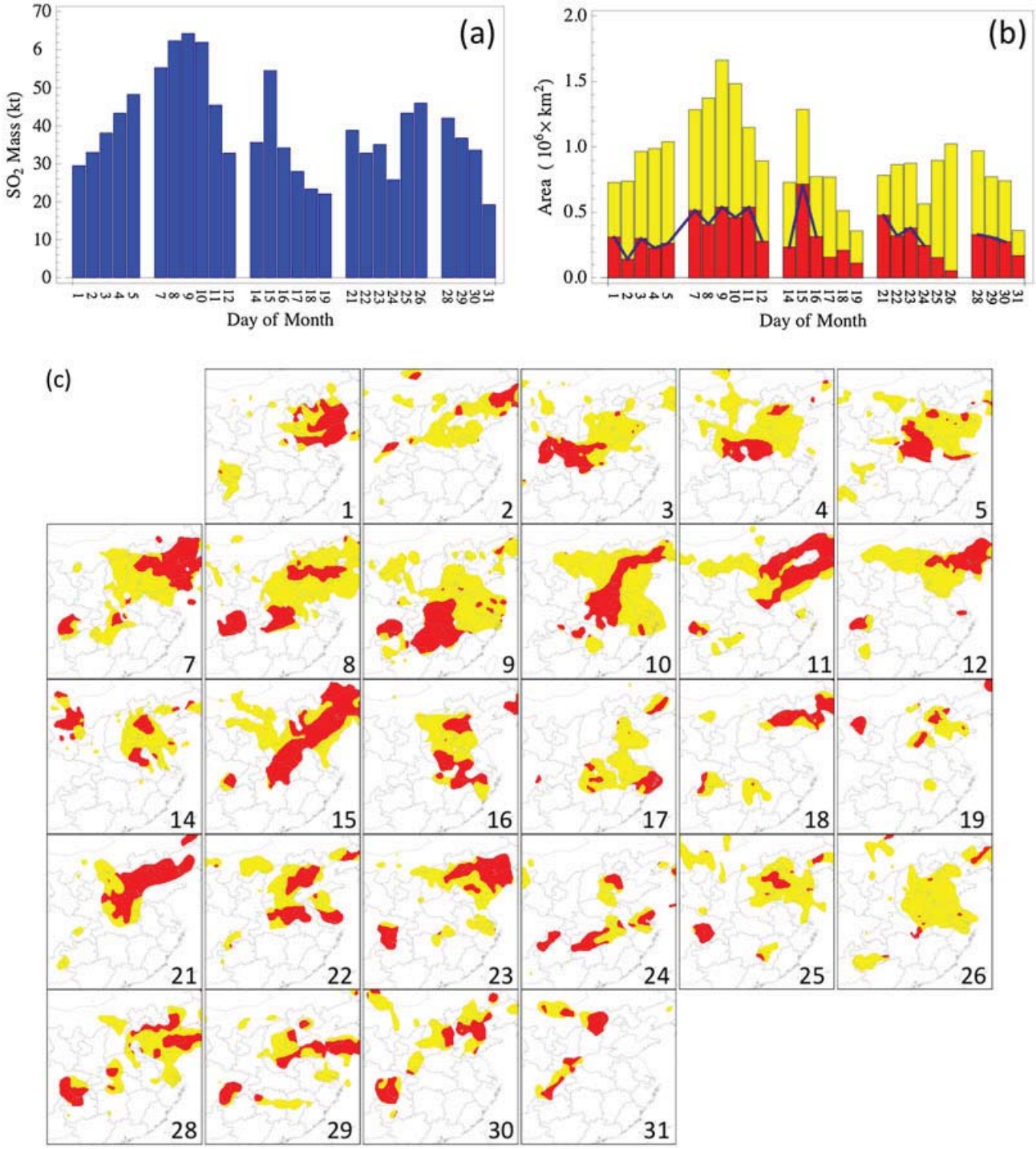

Figure 2. (a) Observed SO_2 masses (kilotons) and (b) SO_2 covered areas (million square kilometers) within the square-bounding box shown in Figure 1, for each day (except Sunday) in January 2013. Results on Sundays are not shown, because OMPS NM is operated in a high-spatial resolution mode, with a reduced spectral coverage. The daily mass is the sum of all SO_2 values in the bounding box for the day, but areas are calculated for high SO_2 (>0.5 DU) regions, i.e., the sum of the yellow and red zones in the corresponding map in Figure 2c. (c) The red zones are defined as smog-covered areas, in which both SO_2 and the UV aerosol index (AI) are high (i.e., SO_2 > 0.5 DU and AI >1), and the yellow zones are high SO_2 and low AI areas (SO_2 > 0.5 DU and AI < 1).

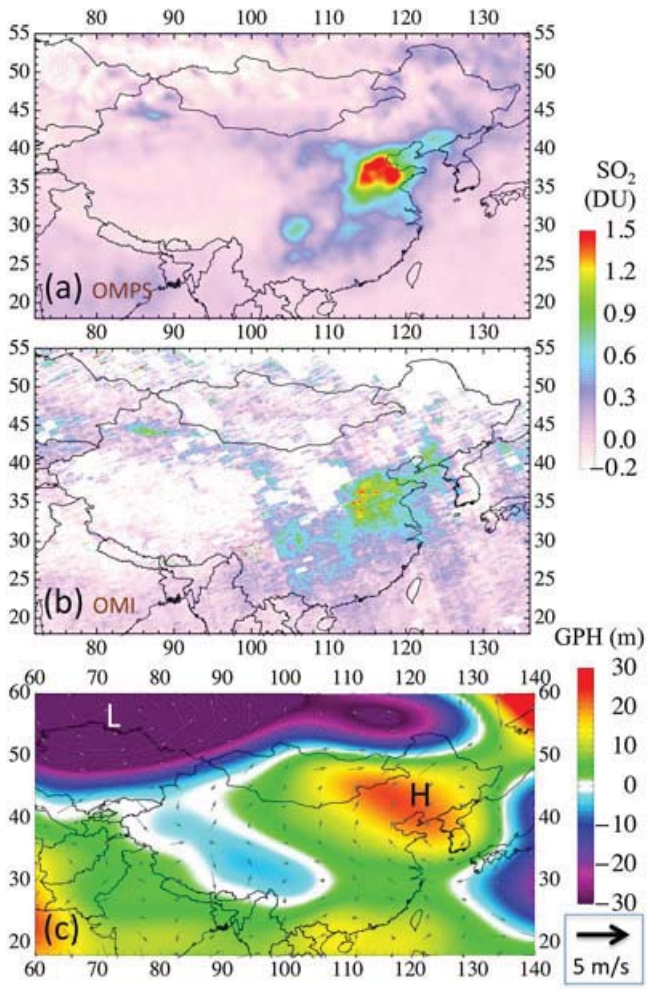

Figure 3. (a) The average SO_2 VCD map measured by SNPP/OMPS NM with MLER cloud fraction less than 50% over East Asia for January 2013, (b) the corresponding SO_2 map composited with the lower tropospheric SO_2 column (ColumnAmountSO2_TRL) of the operational OMI SO_2 product, and (c) the 500 hPa geopotential height (GPH) anomaly and 700 hPa wind vector anomaly (with respect to the 1980–2010 means) for January 2013. Letters "L" and "H", respectively, indicate the negative and positive geopotential anomalies. The highest OMPS SO_2 VCD is 1.65 DU, located at (118.3°E, 36.8°N), and the OMI SO_2 VCD is 0.8 DU at this location. Note that the OMPS map includes observations from its full swath, while the OMI map (Figure 3b) is produced with cross-track samples 1 to 21 (out of 1 to 60) to avoid the effect of the row anomaly (see http://www.knmi.nl/omi/research/product/rowanomaly-background.php).

derived from the lower tropospheric (TRL) SO_2 VCDs (ColumnAmountSO2_TRL in the operational OMI product, OMSO2). The OMI TRL SO_2 VCDs are derived using the linear fit (LF) algorithm [*Yang et al.*, 2007], with a near uniform a priori SO_2 profile from the ground to about 5.5 km above sea level. Similar spatial distributions of elevated SO_2 are exhibited in Figures 3a and 3b, with the OMI TRL SO_2 VCDs mostly lower than the corresponding OMPS ISF values. The lower TRL SO_2 columns are expected due to the generally higher center of mass of the a priori profiles relative to the climatological profiles [*Lee et al.*, 2009] used in OMPS ISF retrievals. This comparison also shows that OMI detects more of the SO_2 transport away from the sources, as illustrated in Figure 3b with elevated SO_2 values distributed further east, away from the coast of China, primarily due to OMI's smaller pixel sizes that are more capable of seeing through broken clouds. These consistent spatial distributions of SO_2, obtained using different (ISF and LF) algorithms from independent satellite measurements, provide an indirect validation of the new OMPS NM retrievals.

4. Summary

[13] We have shown that OMPS NM provides high-quality PBL SO_2 measurements, characterized by low biases (within ±0.2 DU) in both along- and cross-track directions of the orbital swaths and by high precision (~0.2 DU) for its IFOVs. The OMPS measurements are about 7 times more precise than the current operational OMI PBL SO_2 retrievals, which have a ~1.5 DU noise level [*Krotkov et al.*, 2008]. The improved SO_2 measurements are made possible by the unique instrument design that provides high-quality spectral coverage of the 300–380 nm range using a single CCD detector array and by the stable instrument performance. Both the design and performance facilitate the accurate characterization and effective stray-light corrections of its hyperspectral radiance measurements, which in turn allow the ISF algorithm to take advantage of the high SO_2 sensitivity region below 310 nm. The broader consistent high-quality spectral coverage, coupled with advances in retrieval algorithm and radiance correction techniques, now permit daily global observation of SO_2, with an improved detection limit (precision of ~0.2 DU) for SO_2 in the PBL for its IFOVs. The OMPS NM measurements can detect and quantify much smaller SO_2 amounts (~0.01 DU) with enhanced spatial resolution when averaging the repeated samplings of the same region over time. These improved measurements allow more accurate quantification of atmospheric SO_2 from volcanic emissions and anthropogenic pollution to provide new information on the relative importance of these sources for climate studies.

[14] Using the high-quality OMPS data, we were able to quantify synoptic-scale air pollution events over China in January 2013. The cumulative SO_2 mass measured by OMPS is 1065 kt ($=1.065\times10^{12}$ g = 1.065 Tg). This represents the lower limit of total SO_2 loading within the bounding box (23.1° × 23.1° dashed box in Figure 1) for this month, as SO_2 obscured from the satellite FOV by thick clouds and emissions on Sundays (on which OMPS operates in a mode with reduced spectral coverage) are not measured. This observed SO_2 mass is about half of the total SO_2 emission (~2 Tg) [*Yang et al.*, 2010] from the 2008 Kasatochi eruption (among the largest in the past decade), highlighting that coal combustion in China continues releasing large amounts of SO_2 into the atmosphere, and contributes greatly to the country's air pollution today.

[15] The OMPS NM is designed primarily for measuring O_3 in the upper atmosphere. As demonstrated here, this well-characterized hyperspectral instrument also provides sensitive observations of trace gasses in the PBL. We are developing new capabilities to extract greater and more accurate information from these observations, so that the

quality of OMPS trace gas products is sufficient to match or surpass those of the Aura/OMI environmental data records (EDR). We are on track to achieve this goal, as the next OMPS NM instruments, with an enhanced spatial resolution (12 ×12 km at nadir), will fly on the NOAA and NASA Joint Polar Satellite System (JPSS) spacecraft: JPSS-1 (scheduled to launch in early 2017) and JPSS-2.

[16] **Acknowledgments.** This work is supported by NASA under grant NNX11AK95G (Continuation of Long-Term Sulfur Dioxide EDR with the SNPP/OMPS NM). We acknowledge the use of OMPS Level 1B data produced by the SNPP Ozone Product Evaluation and Algorithm Test Element (PEATE), funded by NASA. The authors thank the editor and the two anonymous reviewers for their suggestions and constructive comments.

[17] The Editor thanks two anonymous reviewers for their assistance in evaluating this paper.

References

Ahmad, Z., P. K. Bhartia, and N. Krotkov (2004), Spectral properties of backscattered UV radiation in cloudy atmospheres, *J. Geophys. Res.*, *109*, D01201, doi:10.1029/2003JD003395.

Bhartia, P. K., and C. W. Wellemeyer (2002), OMI TOMS-V8 Total O_3 Algorithm, in *Algorithm theoretical baseline document: OMI ozone products,* vol. II, edited by P. K. Bhartia, p. 15–31, NASA Goddard Space Flight Center, Greenbelt, Maryland, USA, ATBD-OMI-02, ver. 2.0 [Available at ftp://jwocky.gsfc.nasa.gov/pub/LLM_climatology].

Bovensmann, H., J. P. Burrows, M. Buchwitz, J. Frerick, S. Noël, V. V. Rozanov, K. V. Chance, and A. P. H. Goede (1999), SCIAMACHY: Mission objectives and measurement modes, *J. Atmos. Sci.*, *56*, 127–150, doi:10.1175/1520-0469(1999)056<0127:SMOAMM>2.0.CO;2.

Burrows, J. P., et al. (1999), The Global Ozone Monitoring Experiment (GOME): Mission concept and first scientific results, *J. Atmos. Sci.*, *56*, 151–175, doi:10.1175/1520-0469(1999)056<0151:TGOMEG>2.0.CO;2.

Carn, S. A., A. J. Krueger, N. A. Krotkov, K. Yang, and P. F. Levelt (2007), Sulfur dioxide emissions from Peruvian copper smelters detected by the Ozone Monitoring Instrument, *Geophys. Res. Lett.*, *34*, L09801, doi:10.1029/2006GL029020.

Dickerson, R. R., et al. (2007), Aircraft observations of dust and pollutants over northeast China: Insight into the meteorological mechanisms of transport, *J. Geophys. Res.*, *112*, D24S90, doi:10.1029/2007JD008999.

Eisinger, M., and J. P. Burrows (1998), Tropospheric Sulfur Dioxide observed by the ERS-2 GOME Instrument, *Geophys. Res. Lett.*, *25*, 4177–4180, doi:10.1029/1998GL900128.

Fioletov, V. E., C. A. McLinden, N. Krotkov, M. D. Moran, and K. Yang (2011), Estimation of SO_2 emissions using OMI retrievals, *Geophys. Res. Lett.*, *38*, L21811, doi:10.1029/2011GL049402.

Fleig, A. J., K. F. Klenk, P. K. Bhartia, and D. Gordon (1982), *User's Guide for the Total-Ozone Mapping Spectrometer (TOMS) Instrument First-Year OZONE-T Data Set*, NASA Reference Publication 1096, National Aeronautics and Space Administration, Washington, D. C.

Haagen-Smit, A. J. (1952), Chemistry and physiology of Los Angeles smog, *Ind. Eng. Chem. Res.*, *44*(6), 1342–1346, doi:10.1021/ie50510a045.

He, H., et al. (2012), SO_2 over central China: Measurements, numerical simulations and the tropospheric sulfur budget, *J. Geophys. Res.*, *117*, D00K37, doi:10.1029/2011JD016473.

He, K., H. Huo, and Q. Zhang (2002), Urban air pollution in China: Current status, characteristics, and progress, *Annu. Rev. Energy Environ.*, *27*, 397–431, doi:10.1146/annurev.energy.27.122001.083421.

Heath, D. F., A. J. Krueger, H. A. Roeder, and B. D. Henderson (1975), The Solar Backscatter Ultraviolet and Total Ozone Mapping Spectrometer (SBUV/TOMS) for NIMBUS G, *Opt. Eng.*, *14*(4), 144,323, doi:10.1117/12.7971839.

Hsu, N. C., C. Li, N. A. Krotkov, Q. Liang, K. Yang, and S.-C. Tsay (2012), Rapid transpacific transport in autumn observed by the A-train satellites, *J. Geophys. Res.*, *117*, D06312, doi:10.1029/2011JD016626.

Joiner, J., P. K. Bhartia, R. P. Cebula, E. Hilsenrath, R. D. McPeters, and H.-W. Park (1995), Rotational Raman scattering (Ring effect) in satellite backscatter ultraviolet measurements, *Appl. Opt.*, *34*, 4513–4525, doi:10.1364/AO.34.004513.

Krotkov, N. A., S. A. Carn, A. J. Krueger, P. K. Bhartia, and K. Yang (2006), Band residual difference algorithm for retrieval of SO_2 from the Aura Ozone Monitoring Instrument (OMI), *IEEE Trans. Geosci. Remote Sens.*, *44*(5), 1259–1266, doi:10.1109/TGRS.2005.861932.

Krotkov, N. A., et al. (2008), Validation of SO_2 retrievals from the Ozone Monitoring Instrument over NE China, *J. Geophys. Res.*, *113*, D16S40, doi:10.1029/2007JD008818.

Lee, C., A. Richter, M. Weber, and J. P. Burrows (2008), SO_2 retrieval from SCIAMACHY using the Weighting Function DOAS (WFDOAS) technique: Comparison with standard DOAS retrieval, *Atmos. Chem. Phys.*, *8*, 6137–6145, doi:10.5194/acp-8-6137-2008.

Lee, C., R. V. Martin, A. van Donkelaar, G. OḂyrne, N. Krotkov, A. Richter, L. G. Huey, and J. S. Holloway (2009), Retrieval of vertical columns of sulfur dioxide from SCIAMACHY and OMI: Air mass factor algorithm development, validation, and error analysis, *J. Geophys. Res.*, *114*, D22303, doi:10.1029/2009JD012123.

Levelt, P. F., G. H. J. van den Oord, M. R. Dobber, A. Mälkki, H. Visser, J. de Vries, P. Stammes, J. O. V. Lundell, and H. Saari (2006), The Ozone Monitoring Instrument, *IEEE Trans. Geosci. Remote Sens.*, *44*(5), 1093–1101, doi:10.1109/TGRS.2006.872333.

Munro, R., M. Eisinger, C. Anderson, J. Callies, E. Corpaccioli, R. Lang, A. Lefebvre, Y. Livschitz, and A. Perez Albinana (2006), GOME-2 on MetOp, paper presented at the *2006 EUMETSAT Meteorological Satellite Conference*, Eur. Org. for the Exploit of Meteorol. Satell., Helsinki.

Nowlan, C. R., X. Liu, K. Chance, Z. Cai, T. P. Kurosu, C. Lee, and R. V. Martin (2011), Retrievals of sulfur dioxide from the Global Ozone Monitoring Experiment 2 (GOME-2) using an optimal estimation approach: Algorithm and initial validation, *J. Geophys. Res.*, *116*, D18301, doi:10.1029/2011JD015808.

Tao, M., L. Chen, L. Su, and J. Tao (2012), Satellite observation of regional haze pollution over the North China Plain, *J. Geophys. Res.*, *117*, D12203, doi:10.1029/2012JD017915.

Thorsheim, P. (2009), *Inventing Pollution: Coal, Smoke, and Culture in Britain since 1800 (Ecology & History)*, Ohio University Press, Athens. Jun 15, 2009.

U.S. Energy Information Administration (2012), China Report, September 4, 2012. [Available at: http://www.eia.gov/countries/analysisbriefs/China/china.pdf].

Wang, J., X. Xia, P. Wang, and S. A. Christopher (2004), Diurnal variability of dust aerosol optical thickness and Angstrom exponent over dust source regions in China, *Geophys. Res. Lett.*, *31*, L08107, doi:10.1029/2004GL019580.

Yang, K., N. A. Krotkov, A. J. Krueger, S. A. Carn, P. K. Bhartia, and P. F. Levelt (2007), Retrieval of large volcanic SO_2 columns from the Aura Ozone Monitoring Instrument: Comparison and limitations, *J. Geophys. Res.*, *112*, D24S43, doi:10.1029/2007JD008825.

Yang, K., N. A. Krotkov, A. J. Krueger, S. A. Carn, P. K. Bhartia, and P. F. Levelt (2009), Improving retrieval of volcanic sulfur dioxide from backscattered UV satellite observations, *Geophys. Res. Lett.*, *36*, L03102, doi:10.1029/2008GL036036.

Yang, K., X. Liu, P. K. Bhartia, N. A. Krotkov, S. A. Carn, E. J. Hughes, A. J. Krueger, R. J. D. Spurr, and S. G. Trahan (2010), Direct retrieval of sulfur dioxide amount and altitude from spaceborne hyperspectral UV measurements: Theory and application, *J. Geophys. Res.*, *115*, D00L09, doi:10.1029/2010JD013982.